Large-Scale Silicon Photonic Circuits for Optical Phased Arrays

Jie Sun, *Member, IEEE,* Erman Timurdogan, *Student Member, IEEE,* Ami Yaacobi, Zhan Su,
Ehsan shah Hosseini, David B. Cole, and Michael R. Watts, *Member, IEEE,*

(Invited Paper)

Abstract—We review recent advances in integrated large-scale optical phased arrays. The design and fabrication of large-scale optical phased arrays using silicon photonic circuits are discussed from device designs including the directional couplers, thermo-optic phase shifters, and optical nanoantennas, to system studies including phased array synthesis and noise analysis. By taking advantage of the well-developed silicon complementary metal-oxide-semiconductor (CMOS) fabrication technology, several large-scale integrated silicon photonic phased arrays are demonstrated, including two passive phased arrays (64×64 and 32×32) with the ability to generate complex holographic images, an 8×8 active phased array for dynamic optical beamforming, and an 8×8 active antenna array with amplitude apodization. These optical phased array demonstrations, with up to 12,000 integrated optical elements, represent the largest and densest silicon photonic circuits demonstrated to date.

Index Terms—Silicon photonics, integrated optics, photonic integrated circuits, nanophotonics, phased arrays.

I. INTRODUCTION

THE Nobel Laureate Karl Ferdinand Braun stated in his Nobel lecture in 1909 that he had dreamt of a device that can "transmit the waves, in the main, in one direction only" [1], [2]. The device Braun was referring to was later known as the phased array, which uses the relative phase of an array of antennas to reshape the radiation field of the electromagnetic waves through constructive and destructive interferences. The microwave version of Braun's dream, namely the radio-frequency phased array, came true in the midst of World War II [3] and has since then been widely deployed around the world for applications ranging from communication to object detection to astronomy [4]. The optical version, *i.e.* the optical phased array, made its debut shortly after the invention of laser, and has hitherto been extensively researched using a variety of platforms [5], including bulk optics [6], liquid crystals [7], optical fibers [8], III-V laser arrays [9], optical waveguides [10], microelectromechanical systems (MEMS) [11], *etc.* It is,

however, less developed compared to its microwave counter-part because of the difficulty to manipulate the much shorter optical wavelength, which was well recognized by Braun more than a century ago [1].

High-resolution optical phased arrays require a large number of optical antennas be placed close to each other two dimensionally - ideally on the order of the optical wavelength - to reduce the number of interference orders in the far field [12]. In addition, 2π optical phase tunability needs to be provided for each optical antenna to actively reshape the far-field radiation. These stringent requirements present key challenges to the design and fabrication of optical phased arrays. Recently, *Yu et al.* [13] and many others [14] demonstrated a method to engineer the optical phase through the shape and orientation of densely packed surface plasmonic nanoantennas. While this method can meet the antenna spacing requirement, it has limitations that active phase tunability would be hard to implement for individual antenna in such a free-space optical device. To incorporate active phase tunability, *Guo et al.* [15] utilized indium phosphide (InP) integrated circuit and built a one-dimensional (1×8) optical phased array, which, however, is difficult to extend to larger-scale two-dimensional arrays.

Alternatively, silicon photonic circuits take advantage of many of the well-established CMOS processing techniques so successful in producing advanced, densely integrated microelectronics; in addition, silicon has versatile phase-tuning mechanisms such as the efficient thermo-optic effect [16] and the fast plasma dispersion effect [17]. These advantages make the silicon photonic circuit a promising candidate to address the aforementioned stringent design and fabrication challenges in optical phased arrays. Several optical phased arrays using silicon photonic circuits have been demonstrated. *Van Acoleyen et al.* [18] first demonstrated a two-dimensional 4×4 passive optical phased array with 60 μm antenna spacing, where the generated optical beam can be steered in one dimension through wavelength sweeping. *Doylend et al.* [19] built a 1×16 optical phased array with thermo-optic phase tuning through over-cladded metal heaters. *Doylend et al.* [20] continued to integrate III/V components on the silicon photonic phased array chip for light generation and amplification, realizing the first self-contained silicon photonic phased array without any off-chip component. These previous achievements, implemented in a relatively small scale with no more than 16 antennas, represented excellent early demonstrations; however, the architectures adopted in these phased arrays are not scalable to large-scale two-dimensional arrays due to the
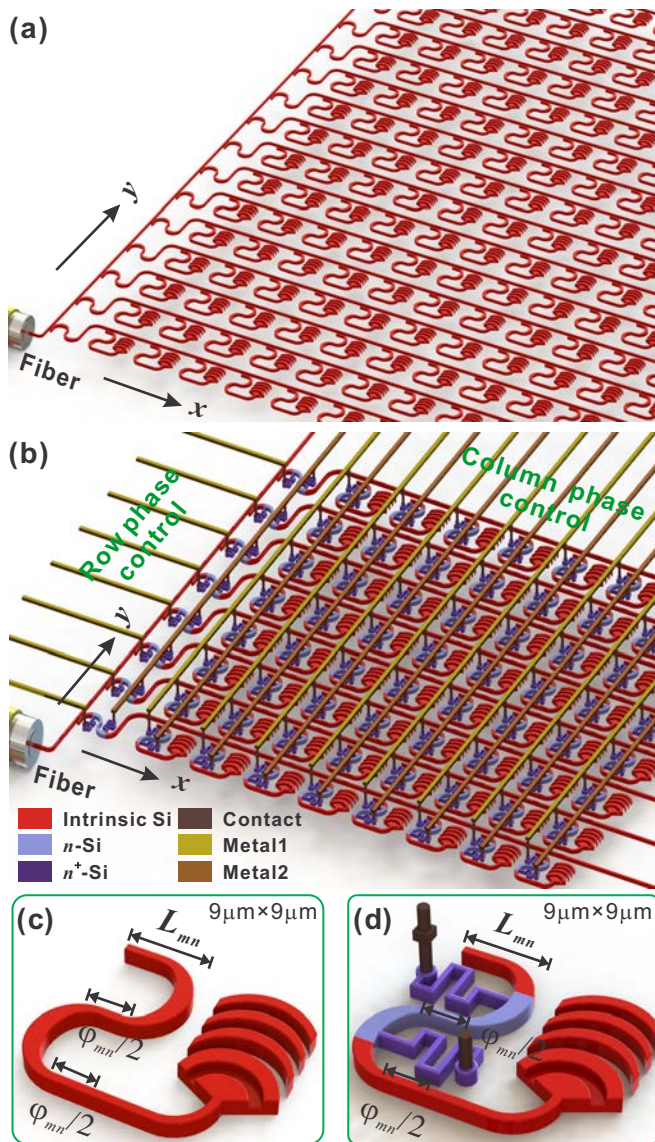
Fig. 1. The architecture of the large-scale integrated optical phased array on the silicon photonic platform. (a) The passive phased array. (b) The active array. (c) A passive unit cell, and (d) an active unit cell of the optical phased array, consisting of a directional coupler, an optical phase shifter with active phase tunability, and a dielectric nanoantenna. Figs. reproduced with permission from [21], ©2013 NPG.

both optical phased array and silicon photonic integration. Aside from it being the largest optical phased array, the demonstration shows the large-scale integration of photonic circuitry in silicon has well and truly arrived [2].

This paper presents a systematic study of the large-scale integrated optical phased array using this novel architecture together with the advanced silicon photonic fabrication platform. The rest of the paper is organized as follows. Section II discusses the device-level building blocks of the optical phased array, including the directional coupler as the optical power splitter, the integrated thermo-optically tunable phase shifters, and the efficient dielectric optical nanoantenna, all of which are integrated in a compact unit cell. Section III studies the system-level antenna synthesis and analysis for this large-scale coherent optical system. Section IV presents the experimental results, including two large-scale passive arrays (64×64 and 32×32), an active 8×8 array, and an 8×8 antenna array with amplitude apodization. The CMOS processing technique that enables this large-scale silicon photonic fabrication is also discussed in Section IV. Section V gives concluding remarks.

II. DEVICES: ANTENNA UNIT CELL

Fig. 1(a) illustrates the architecture of an $M \times N$ integrated optical phased array using the large-scale silicon photonic circuit, and Fig. 1(b) shows an active array with thermo-optic phase tunability. The laser input is launched from an optical fiber into a silicon bus waveguide. The optical power in the silicon bus waveguide is divided into M silicon row waveguides through M directional couplers, and the light in each silicon row waveguide is then coupled into N unit cells through another N directional couplers. In this way, the $M \times N$ optical phased array can be fed with arbitrary optical power distributions by properly designing the directional couplers. Each unit cell, as shown in Fig. 1(c) and Fig. 1(d), is composed of three silicon photonic components: a directional coupler to unload precise amounts of optical power from the feeding bus waveguide, an optical phase shifter with active phase tunability, and a dielectric nanoantenna to emit light from the waveguide to the surrounding medium where light interferes. In optical phased array, it is critical to make the size of the unit cell as small as possible in order to reduce high-order interferences in the far field. Benefiting from the high-index-contrast of silicon and the advanced photonic design, both the passive unit cell and the active unit cell in this work have a compact footprint of 9 μm×9 μm, representing the smallest antenna spacing in two-dimensional integrated optical phased arrays demonstrated so far. Fig. 2 shows the scanning-electron micrograph (SEM) of a fabricated passive unit cell. In this section, we will discuss in detail the three silicon photonic components that form the compact unit cell.

difficult two-dimensional waveguide routing and optical phase matching issues.

Recently we proposed and demonstrated a novel phased array architecture where the waveguide routing and phase matching issues are completely circumvented so that there exists no obstacles to build a two-dimensional optical phased array with millions of antennas [21]. The key advantage of this architecture lies in its ability to integrate an optical directional coupler, a 2π tunable phase shifter, and a dielectric optical nanoantenna within a compact 9 μm×9 μm unit cell using CMOS-compatible silicon photonic process. This architecture, combined with the powerful CMOS processing techniques, enables the demonstration of large-scale optical phased arrays up to 64×64, consisting of 4,096 antenna unit cells or 12,288 functional silicon photonic components, a record number for

A. Directional Coupler

The directional coupler evanescently couples light from the silicon bus waveguide to the row waveguides, and from the row waveguide to the unit cells, as shown in Fig. 1. The power-coupling coefficient η of the directional coupler is adjusted by two parameters: the coupling length (L) and the coupling gap
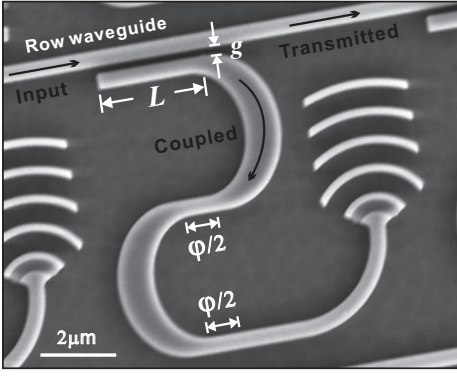
Fig. 2. The scanning- electron micrograph (SEM) of a fabricated passive unit cell. Fig. 2 reproduced with permission from [21], ©2013 NPG.

(g) between the coupler and the bus waveguide. The coupling length should be short enough to fit in the compact unit cell, and the coupling gap should be larger than the critical dimension allowed by the fabrication which is 100 nm in our fabrication process. Using a rigorous three-dimensional (3D) finite-difference in time-domain (FDTD) simulation, the power-coupling coefficient at different coupling length and coupling gap was calculated in Fig. 3(a). The power-coupling coefficient changes from 0.04% to 68% when the coupling length varies between 0.5 μm to 5.2 μm and the coupling gap varies between 0.14 μm to 0.4 μm. The waveguide width is 0.4 μm for both the bus waveguide and the directional coupler. Different coupling lengths and gaps also cause slight phase variation to the coupled light and transmitted light, which has to be taken into account since the phased array is a phase-sensitive system. Fig. 3(b) and Fig. 3(c) show the phase variation of the coupled and transmitted light at different coupling lengths and gaps.

In an $M \times N$ optical phased array with designed near-field intensity distribution $|w_{mn}|^2$, the power-coupling coefficient of the directional coupler in the unit cell (m, n) is given by

$$\eta_{mn} = \frac{|w_{mn}|^2}{|w_{mN}|^2 + \sum_{j=n}^{N} |w_{mj}|^2} \quad (1)$$

and the coupling coefficient of the directional coupler at the beginning of the mth row waveguide is given by

$$\eta_m = \frac{|w_{mN}|^2 + \sum_{j=1}^{N} |w_{mj}|^2}{|w_{MN}|^2 + \sum_{j=1}^{M} |w_{Mj}|^2 + \sum_{i=m}^{M} (|w_{iN}|^2 + \sum_{j=1}^{N} |w_{ij}|^2)} \quad (2)$$

Using (1) and (2), combined with the FDTD simulation in Fig. 3(a), any near-field emission profile $|w_{mn}|$ can be achieved in the optical phased array utilizing the proposed optical power-delivery network based on the directional couplers. Most optical phased arrays require uniform near-field emission, that is, $|w_{mn}| = 1$ across the whole array. Then the coupling
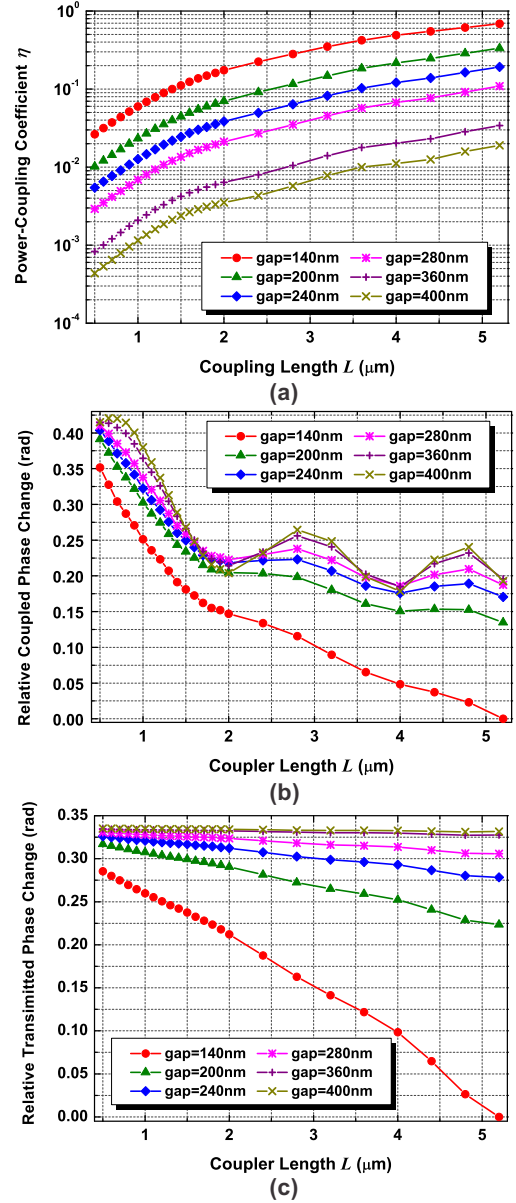

Fig. 3. Design of the directional coupler. (a) The power-coupling coefficient as a function of the coupling length and gap. The relative phase change of (b) the coupled light and (c) the transmitted light at different coupling lengths and gaps.

coefficients in (1) and (2) become

$$\eta_{mn} = \frac{1}{N - n + 2}, \eta_m = \frac{1}{M - m + 2} \quad (3)$$

Note that a small amount of the optical power is discarded at the end of the bus waveguide and each row waveguide so that the coupling coefficient of the last directional coupler is 50%, as calculated in (1) to (3). This avoids coupling out 100% light to the last row waveguide or the last unit cell of each row, which will require an ultra-long coupling length that would not be fit into the unit cell or an ultra-narrow coupling gap that would not be lithographically resolved.
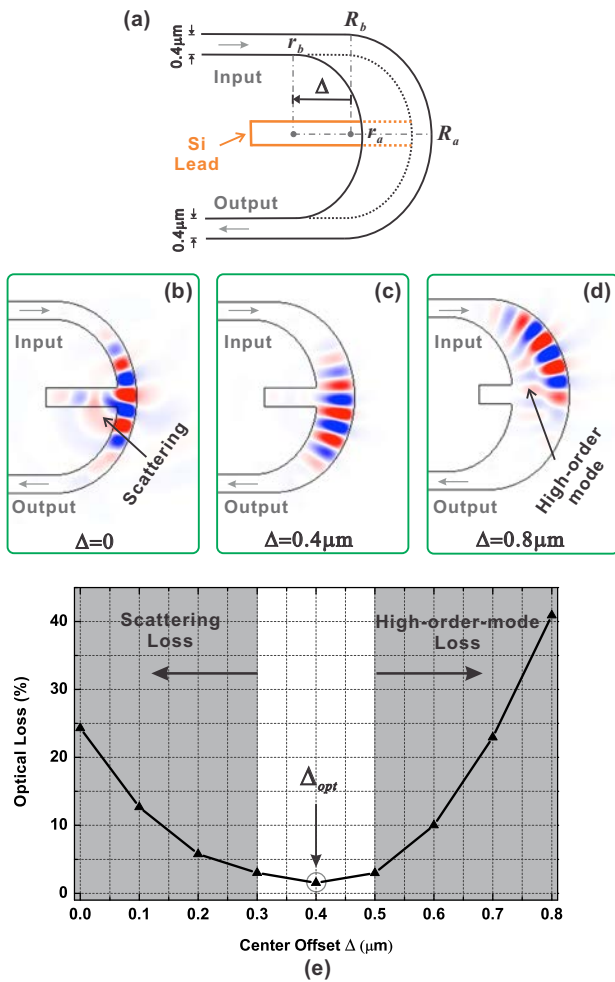
Fig. 4. Tunable phase shifter with adiabatic bend. (a) A schematic of the adiabatic bend in the tunable phase shifter to make low-loss electrical contact. The 3D-FDTD simulation of light passing through a waveguide bend with a silicon lead, where the center of the inner ellipse is offset by different distances Δ to form an adiabatic bend: (b) $\Delta = 0$, (c) $\Delta = 0.4$ μm, and (d) $\Delta = 0.8$ μm. (e) The 3D-FDTD simulation of the optical loss from the adiabatic bend with an attached silicon lead. The optimal offset is $\Delta_{opt} = 0.4$ μm.

B. Optical Phase Shifter

The optical phase shifter provides an accurate relative phase φ to the optical antenna. This phase shift is introduced statically by two identical optical delay lines, each of which delays the optical phase by $\varphi/2$, as shown in Fig. 2. This configuration ensures the antenna position is independent on the phase shift required in the unit cell, so that the optical antennas in the array can be easily aligned with the two-dimensional periodic grid of the phased array. Using the optical delay lines, each of the unit cells in the optical phased array can be assigned with an accurate emitting phase φ_{mn} that is fixed once the phased array is fabricated.

In addition to the fixed phase shifter, it is more desirable to have a tunable phase shifter where the optical phase can be actively adjusted to achieve 2π tuning range within each compact unit cell. Moreover, since there exist a large number of unit cells in a large-scale phased array, it is critical for the phase shifter to be power-efficient to reduce the power density on the photonic chip. Thermo-optically tunable phase

shifters have been widely used in silicon photonics [22]–[24] to obtain a large phase shift, most of which utilize the over-cladded metal heater that is separated from the waveguide by a layer of dielectric to prevent excessive optical loss from the metal. However, this dielectric layer, sandwiched between the metal heater and waveguide as a large heat capacitor, makes the thermo-optic tuning slower and less power-efficient, preventing compact phase shifters from being implemented. To overcome this challenge, thermo-optic heaters can be directly formed with the silicon waveguide [25]–[29], enabling much more efficient heating in a highly compact phase shifter that fits within the unit cell. As shown in Fig. 1(d), the integrated heater is formed by doping the silicon waveguide to create a resistive heater, and the heater is electrically connected to the metals through a silicon nanowire lead that is directly attached to the silicon waveguide. The silicon waveguide is lightly doped to provide a considerable resistance and to avoid significant optical loss from the dopants. The silicon lead is heavily doped to reduce the contact resistance so that most of the heating power drops on the waveguide; in addition, the zigzagged structure of the silicon lead increases its length and therefore provides better thermal isolation between the high-temperature waveguide and the metal contact, preventing the metal contact from melting at high heating power.

The directly integrated silicon heater gives the most power-efficient thermo-optic phase tuning since the waveguide itself has the highest temperature; however, the intimate contact of the silicon lead with the optical waveguide could cause severe optical losses due to light scattering. As shown by the FDTD simulation in Fig. 4(b), substantial scattering loss is observed when light is passing through a waveguide bend with a directly connected silicon lead. Fortunately, this contact issue was solved by our recently developed adiabatic bend structure [30], which enables low-loss contact with integrated heaters [25]–[28] as well as p-n junctions [31] in various silicon photonic devices. Fig. 4(a) illustrates the adiabatic bend used in this work. The outer edge of the waveguide bend follows an elliptical curve with $R_a = 1.7$ μm and $R_b = 2.0$ μm. The inner edge is also an ellipse with $r_a = 1.3$ μm and $r_b = 1.7$ μm. The centers of the two ellipses are offset by distance Δ. This offset gradually, or adiabatically, widens the central part of the bend, and the silicon lead is introduced in the widened part of the bend where it sees little optical field. In this way, the scattering from the silicon lead is greatly reduced, as shown in Fig. 4(c). However, when the offset is too large, high-order modes will be excited since the waveguide widening is too abrupt to be considered as an adiabatic transition, causing excessive radiation loss, as simulated in Fig. 4(d). As a result, there exists an optimal offset distance Δ_{opt} that causes the lowest loss. Fig. 4(e) simulates the optical loss of the adiabatic bend at different offset distances, where it shows the optimal offset is $\Delta_{opt} = 0.4$ μm, corresponding to a width of 0.8 μm in the center of the adiabatic bend. The scattering loss dominates when the offset is smaller than 0.4 μm, while the excitation of high-order modes is responsible for the loss when the offset is larger than 0.4 μm. The optical loss due to the silicon lead is 1.5% at the optimal point. The material loss caused by the lightly doped waveguide is about 3 dB/mm at a
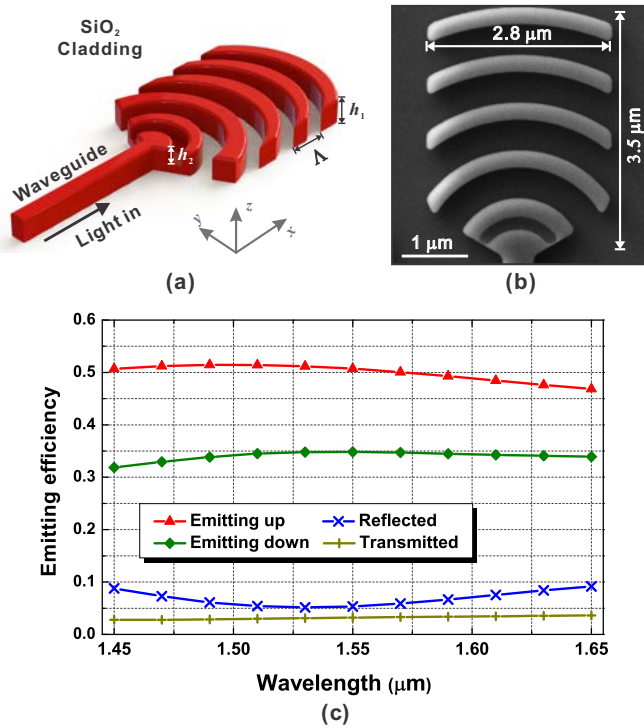
Fig. 5. (a) A schematic of the dielectric optical nanoantenna. (b) An SEM of the fabricated dielectric optical nanoantenna which measures 2.8 µm×3.5 µm. (c) The optical emitting efficiency of the dielectric nanoantenna, calculated from the 3D-FDTD simulation.
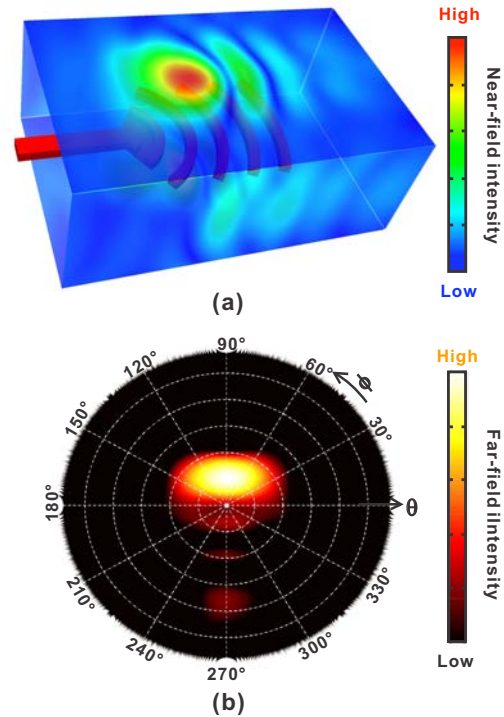

Fig. 6. (a) The near-field emission of the dielectric nanoantenna, calculated with a rigorous 3D-FDTD method. (b) The far-field emission profile of the nanoantenna, $S(\theta, \phi)$, calculated by the near-to-far-field transformation using the optical near field in (a). The far field radiation profile is viewed from the zenith of the far-field hemisphere, as a projection of the far-field hemisphere to the equatorial plane in the polar coordinate system (θ, ϕ). θ and ϕ are the far-field azimuth angle and polar angle, respectively. Figs. reproduced with permission from [21], ©2013 NPG.

typical *n*-type doping level 1×10^{18} cm^{-3} [17], corresponding to a negligible propagation loss of less than 0.5% in the sub-10 µm doping region. Therefore, a high-efficiency, low-loss thermo-optically tunable phase shifter is now made possible through the directly integrated silicon heater and the adiabatic bend.

C. Dielectric Nanoantenna

The optical nanoantenna emits the guided light in the silicon waveguide to the surrounding medium in which free-propagating light interferes in the far field. Preferably, the nanoantenna used in the optical phased array should have high emitting efficiency yet a small size to fit into the compact unit cell. Various efficient wavelength-scale optical nanoantennas have previously been demonstrated in metal [32]–[34] since the large refractive index of metal results in strong light-matter interaction. However, the metallic optical nanoantenna, which requires high-resolution patterning on the metal layer, is not compatible with current CMOS-comptatible silicon photonic process. Therefore, dielectric optical nanoantenna is preferred in the large-scale optical phased array in order to take advantage of the advanced CMOS processing techniques.

In this work, we used the silicon-based dielectric optical antenna, as illustrated in Fig. 5(a). The large refractive index contrast between silicon (*n*=3.48) and SiO₂ cladding (*n*=1.45) creates relatively strong light-matter interaction and hence high emitting efficiency is achievable. Fig. 5(b) shows an SEM of the fabricated silicon nanoantenna with a compact footprint

of 2.8 µm×3.5 µm. The nanoantenna consists of 5-period circular gratings that diffract light from the waveguide to the surrounding SiO₂ cladding. The grating pitch Λ is 0.72 µm, which is slightly detuned from the pitch of a second-order grating to avoid severe resonant back-reflections that would disturb the phased array system. The depth of the grating is h_1=0.22 µm, except for the first period that is partially etched (h_2=0.11 µm) to break the up-down symmetry of the structure so that more optical power is emitting up than emitting down. This is because the partially etched thin silicon slab creates a phase difference between the up-emitting light and down-emitting light in the first grating period so that the up-emission is reinforced through constructive interference while the down-emission is suppressed through destructive interference [35], [36]. Using the rigorous 3D-FDTD simulation, the light emitting efficiency was calculated, as shown in Fig. 5(c). An efficient 51% up-emission is achieved while 35% is emitting down at 1.55 µm wavelength, thanks to the asymmetric grating structure. The up-emission efficiency can be further improved by depositing a layer of polycrystalline silicon on top of the grating to increase the asymmetry of the structure [35]. Only 5% optical power is reflected back to the waveguide because of the detuning of the grating pitch. It is also noted that the emission from the nanoantenna is broadband, with a bandwidth extending across hundreds of nanometers in wavelength. This broadband nature comes from the short length of the grating

and could find potential applications in other nanophotonic devices such as vertical couplers.

The near-field optical emission of the silicon nanoantenna was simulated with the 3D-FDTD method, as shown in Fig. 6(a). The corresponding far-field radiation profile, $S(\theta, \phi)$, was calculated in Fig. 6(b) using the near-to-far-field transformation [37]. The far-field emission is not vertical but centered about $15°$ from the zenith, since the grating pitch is purposely detuned from that of a second-order grating that would emit vertically.

The three components that construct a compact $9~\mu m \times 9~\mu m$ unit cell have now been developed. The unit cell, as the building block of the optical phased array, is to be arrayed to form a large-scale silicon photonic phased array system, where the emitting phase of each unit cell is accordingly adjusted to generate sophisticated optical far-field radiation, as will be discussed in the next section.

III. SYSTEM: ANTENNA SYNTHESIS AND ANALYSIS

The phased array, either in optical frequency or in radio frequency, is conventionally used to form and steer simple far-field radiation patterns such as focused electromagnetic beams. The optical phased array, benefiting from the large-scale silicon photonic integration technology, has the unique opportunity to integrate thousands or even millions of elements in a compact, low-cost chip. By incorporating a large number of optical antennas, complex radiation patterns can be generated, extending the functionalities of phased arrays well beyond the conventional beamforming and steering. This section will discuss the phased array synthesis method to generate designed radiation patterns with large-scale optical phased arrays, as well as noise analysis in such a large-scale coherent optical system.

A. Antenna Synthesis

The electromagnetic radiation $E(\theta, \phi)$ of an $M \times N$ phased array in the far field is given by [38]

$$E(\theta, \phi) = S(\theta, \phi) \times AF(\theta, \phi) \qquad (4)$$

where θ and ϕ are the far-field azimuth angle and polar angle, respectively. The first term $S(\theta, \phi)$ represents the far field of a single antenna, as shown in Fig. 6(b). The second term $AF(\theta, \phi)$ is a scalar called array factor, which is related to the configuration of the phased array through the Fourier transform (denoted by "$\mathfrak{F}$")

$$AF(\theta, \phi) = \sum_{m=1}^{M} \sum_{n=1}^{N} w_{mn} \cdot e^{j2\pi(x_m \cdot u + y_n \cdot v)} = \mathfrak{F}(w_{mn}) \quad (5)$$

where (x_m, y_n) is the coordinate of each nanoantenna, while (u, v) describes the far-field position where $u = \sin(\theta)\cos(\phi)/\lambda$ and $v = \sin(\theta)\sin(\phi)/\lambda$, and λ is the optical wavelength in the medium where light propagates and interferes. w_{mn} represents the optical emission of an individual unit cell, consisting of amplitude and phase, that is, $w_{mn} = |w_{mn}| \cdot e^{j\varphi_{mn}}$.

Since the radiation pattern of a single antenna $S(\theta, \phi)$ is fixed, the phased array synthesis is to find the near-field amplitude $|w_{mn}|$ and phase φ_{mn} that can generate a given array
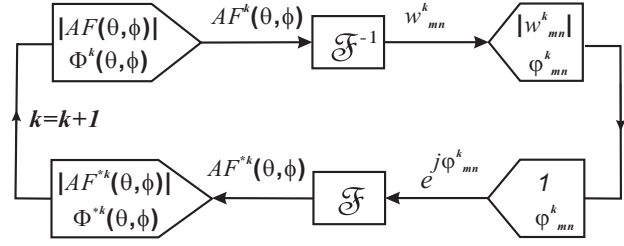

Fig. 7. The block diagram of the Gerchberg-Saxon algorithm for phased array synthesis.

factor in the far field. Equation (5) reveals that the near-field emission w_{mn} can be easily obtained through a simple Fourier transform once the desired far-field array factor $AF(\theta, \phi)$ is given. The required emission amplitude distribution $|w_{mn}|$ is then achieved by the directional couplers according to (1) and (2), and the optical phase φ_{mn} is engineered by the phase shifters in the unit cell. However, most phased arrays, as their name would suggest, use only the phase φ_{mn} to control the far-field radiation while the amplitude is uniform across the array ($|w_{mn}|=1$), which imposes a constraint on the array synthesis. In addition, most phased-array applications focus only on the amplitude $|AF(\theta, \phi)|$ of the far-field radiation. Under such circumstances, the Gerchberg-Saxon algorithm [39], [40] can be utilized here for the phased array synthesis. Fig. 7 illustrates the iterative Gerchberg-Saxon algorithm to synthesize a far-field array factor with amplitude $|AF(\theta, \phi)|$ under uniform near-field emission. At the kth iteration, an approximated array factor $AF^k(\theta, \phi)$ that consists of the targeted amplitude $|AF(\theta, \phi)|$ and a trial phase $\Phi^k(\theta, \phi)$ is inversely Fourier-transformed to find the corresponding near-field optical emission w_{mn}^k. As mentioned above, only the amplitude of the far-field array factor is of interest while its phase $\Phi^k(\theta, \phi)$ can be arbitrarily chosen. The amplitude of the near-field emission is then set to 1 ($|w_{mn}^k|=1$) while its phase φ_{mn}^k remains so that uniform emission is kept across the array. The resulting array factor $AF^{*k}(\theta, \phi)$ is updated through a Fourier transform whose phase $\Phi^{*k}(\theta, \phi)$ is then passed to the $(k+1)^{th}$ iteration as the new trial phase $\Phi^{k+1}(\theta, \phi)$. The initial trial phase is set to $\Phi^1(\theta, \phi)=0$ or any arbitrary values in the first iteration. After several iterations, the final array factor $AF^{*k}(\theta, \phi)$ generated by the near-field phase φ_{mn}^k converges to the desired pattern $|AF(\theta, \phi)|$.

As examples of the Gerchberg-Saxon method, two far-field array factor patterns were synthesized. Fig. 8(a) simulated the far-field array factor pattern of a 64×64 phased array to generate the MIT-logo, and the original MIT-logo is also shown in the lower right. The corresponding phase distribution was calculated in Fig. 8(c). The far field is plotted in the polar coordinate (θ, ϕ), in which the radiation pattern is distorted close to the edge of the coordinate. Fig. 8(b) shows the simulated far field of a 32×32 phased array to produce a concentric multibeam pattern, and the retrieved phase distribution is shown in Fig. 8(d). Note that the antenna spacing was assumed to be $\lambda/2$ in these simulations to avoid high-order interferences.
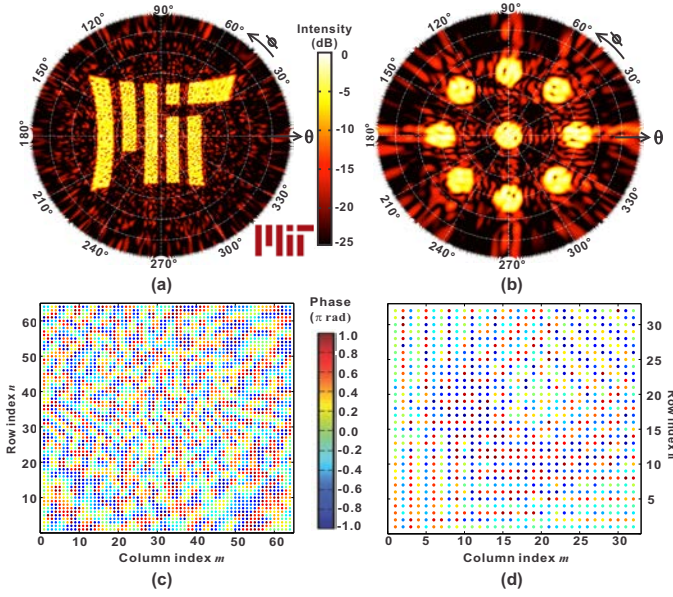
Fig. 8. Phased array synthesis. (a) The simulated far-field pattern of a 64×64 phased array to generate the MIT-logo. The original MIT-logo is shown in the lower right corner. (b) The simulated far-field pattern of a 32×32 phased array to produce a concentric multibeam pattern. (c) The near-field phase distribution φ_{mn}, retrieved by the Gerchberg-Saxon algorithm, of the 64×64 phased array corresponding to the far-field pattern in (a). (d) The near-field phase distribution of the 32×32 phased array corresponding to the far-field pattern in (b).

Fig. 9. Simulated far-field array factor patterns of the 64×64 phased array at different phase-noise levels with standard deviations: (a) $\sigma_p=0$, (b) $\sigma_p=\pi/16$, (c) $\sigma_p=\pi/8$, and (d) $\sigma_p=\pi/4$.

B. Noise Analysis

Theoretically, by precisely assigning a specific optical phase φ_{mn} to each unit cell of the phased array, arbitrary radiation patterns can be generated in the far field. However, it is extremely difficult, if possible, for each unit cell to emit with the exact designed phase in such a large-scale system since the optical phase is very sensitive to fabrication variations due to the short wavelength of light. It is therefore necessary to analyze the performance of the phased array system in the presence of phase noise.

For simplicity, a Gaussian-distributed phase noise ϵ_{mn} was assumed, which is usually the case for noise introduced by fabrication variations. The phase noise has zero mean ($\langle\epsilon_{mn}\rangle=0$) and standard deviation σ_p. The resulting array factor of the far field, $AF^{ac}(\theta,\phi)$, is again given by the Fourier transform of the near-field emission but now with phase noise ϵ_{mn}

$$AF^{ac}(\theta,\phi) = \langle\mathfrak{F}(e^{j\epsilon_{mn}}\cdot w_{mn})\rangle = \langle\mathfrak{F}(e^{j\epsilon_{mn}})\rangle\otimes AF(\theta,\phi) \quad (6)$$

where "$\otimes$" is the convolution operator. The expectation value, denoted by the angle brackets, is used here to represent the stochastic variables. The first term in (6), *i.e.* the Fourier transform of the phase noise, is given by

$$\langle\mathfrak{F}(e^{j\epsilon_{mn}})\rangle = \sum_{m=1}^{M}\sum_{n=1}^{N}\langle e^{j\epsilon_{mn}}\rangle\cdot e^{j2\pi(x_m\cdot u+y_n\cdot v)} \quad (7)$$

And the expectation value of the phase noise in (7) is by definition calculated as

$$\langle e^{j\epsilon_{mn}}\rangle = \int_{-\infty}^{+\infty} e^{j\epsilon}\cdot\frac{1}{\sqrt{2\pi}\sigma_p}e^{-\frac{\epsilon^2}{2\sigma_p^2}}d\epsilon = e^{-\sigma_p^2/2} \quad (8)$$

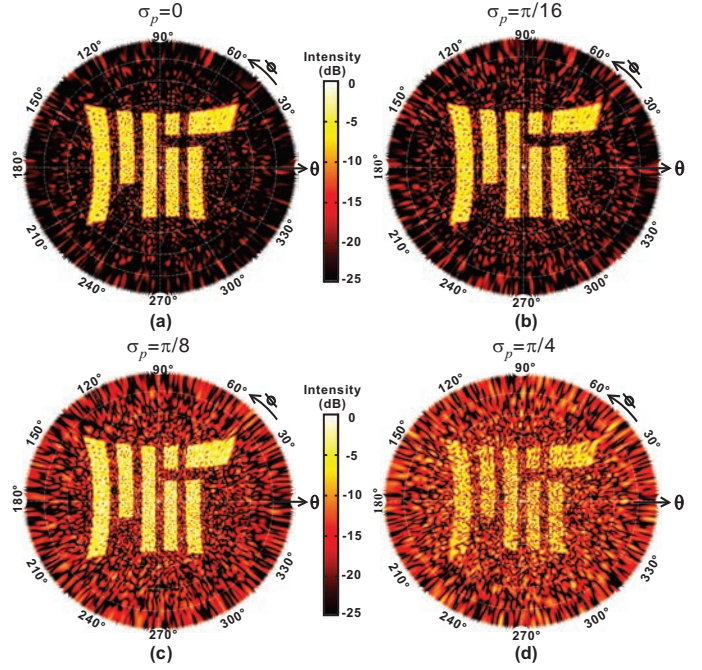Substituting (8) into (7) and then into (6) yields

$$AF^{ac}(\theta,\phi) = e^{-\sigma_p^2/2}\cdot AF(\theta,\phi) \quad (9)$$

Equation (9) reveals that the generated array factor preserves the designed pattern $AF(\theta,\phi)$ in the presence of the phase noise except that its amplitude is reduced by a factor $e^{-\sigma^2/2}$.

To further visualize the effect of the phase noise on the far-field radiation, the array factor patterns were simulated for the aforementioned 64×64 phased array at different phase noise levels (*i.e.* standard deviation σ_p), as shown in Fig. 9. As predicted by the analytical derivations, the shape of the designed image remains unchanged in the presence of the phase noise. As the phase noise level increases, the background noise rises and the signal-to-noise ratio (SNR) of the image decreases, since the ideal interference conditions to generate the designed pattern is no longer completely met due to the phase noise. Nevertheless, even under considerably high noise level with standard deviation $\sigma_p=\pi/4$, the designed MIT-logo pattern is still distinguishable.

In addition to the phase noise, the intensity noise caused by the fabrication variations in the directional couplers also needs to be taken into account. Assuming the coupling coefficients vary with a Gaussian distribution with standard deviation σ_i (in percentage), the resulting far-field array factor patterns $AF_{ac}(\theta,\phi)$ were simulated in Fig. 10. Similar to the phase noise, intensity noise contributes to the background noise but does not change the shape of the designed far-field pattern.

Both the analysis and simulation show that the large-scale phased array is a robust system that is highly tolerant of noise. This ensures the large-scale phased array system be reliably fabricated with moderate fabrication requirements. This robustness originates from the large-scale nature of this
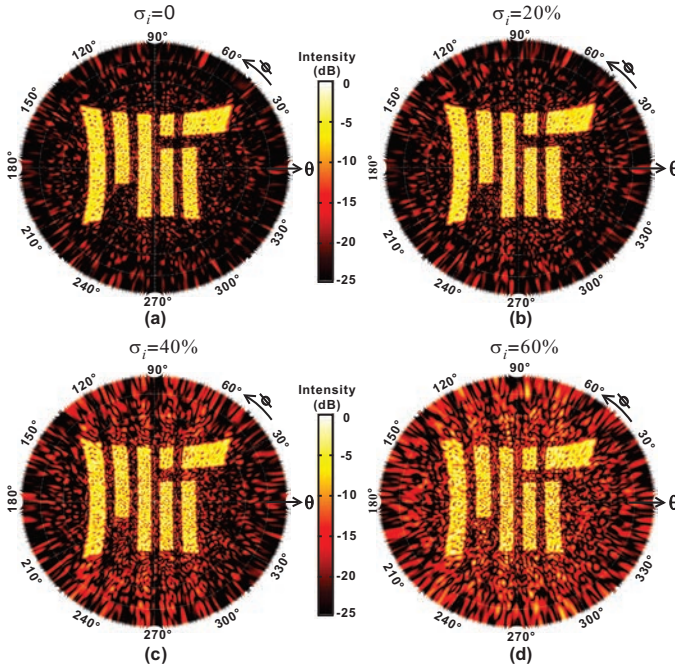
Fig. 10. Simulated far-field array factor patterns of the 64×64 phased array at different intensity-noise levels, represented by the standard deviation of the coupling coefficients of the directional couplers: (a) $\sigma_i=0$, (b) $\sigma_i=20\%$, (c) $\sigma_i=40\%$, and (d) $\sigma_i=60\%$.

coherent system where the random noise cancels out in the far field through the interference from a large number of antennas. Therefore, the more antennas the phased array has, the more robust the system is.

C. High-Order Interference

In the previous simulations, the antenna spacing is assumed to be half of the optical wavelength in the medium, that is, $\Delta x=\Delta y=\lambda/2$. This small antenna spacing, however, is difficult to implement in the optical phased array. When the antenna spacing is much larger than half of the optical wavelength, high-order interference occurs. Assume $\Delta x=\Delta y=P \cdot \lambda/2$, where $P > 1$. According to (5), as $x_m=m \cdot \Delta x$ and $y_n=n \cdot \Delta y$, we have

$$|AF(\theta,\phi)| = |AF(u,v)| = AF(u+\frac{p}{P \cdot \lambda}, v+\frac{p}{P \cdot \lambda}) \quad (10)$$

where p is an integer. Equation (10) suggests that the far-field pattern is replicated with period $\Delta u=\Delta v=1/(P \cdot \lambda)$ in both directions. Since u and v both have the range $(-1/\lambda, 1/\lambda)$, the number of interference orders in the far field is approximately $4P^2$. Fig. 11(a) simulated the far-field array factor pattern with antenna spacing $\Delta x=\Delta y=9$ µm which corresponds to the size of the unit cell in this work. The vacuum wavelength is assumed to be 1.55 µm, which gives $\lambda=1.1$ µm in the SiO$_2$ cladding ($n_{SiO_2}=1.45$) where the light propagates and interferes. Accordingly, P is about 8 in this case. Therefore there are about 16 interference orders in each direction in Fig. 11(a). Again, image distortions are observed close to the edge of the polar coordinate in the plot.

Furthermore, according to (4), we also need to take into account the radiation profile of a single antenna $S(\theta,\phi)$ in
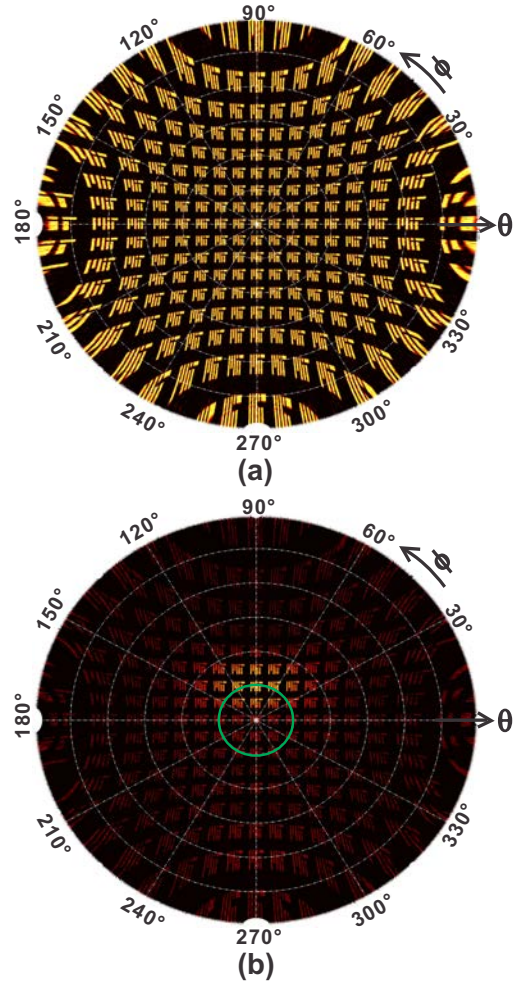

Fig. 11. (a) Simulated far-field array factor patterns of the 64×64 phased array when the antenna spacing is $\Delta x=\Delta y=9$ µm. (b) Simulated far-field radiation pattern $E(\theta,\phi)$ of the 64×64 phased array where the radiation profile of a single antenna is taken into account. The green circle represents the numerical aperture of the lens that will be used in the measurement. Fig. 11(b) reproduced with permission from [21], ©2013 NPG.

order to get the far-field radiation $E(\theta,\phi)$ of the phased array. Fig. 11(b) shows the simulated far-field radiation profile $E(\theta,\phi)$ of the 64×64 phased array with the designed optical nanoantenna, which was obtained by multiplying the array factor pattern (Fig. 11(a)) with the far field of a single antenna (Fig. 6(b)). Obviously the intensity of different interference orders varies from place to place due to the directionality of the optical nanoantenna, and only the orders close to the zenith are visible in the far field.

IV. FABRICATION AND CHARACTERIZATION

In Section III, we have theoretically proved that the large-scale optical phased array is capable of generating complex holographic patterns, a new functionality of phased array that is expected to find potential applications from holography to optical communications to laser detection and ranging (LADAR). However, realizing such a large-scale optical system in a reliable and cost-effective way is challenging yet of great importance to the optical phased array technology. To this end, the silicon photonic circuit, by taking advantage of

the well-developed CMOS processing techniques which have remarkable large-scale integration capability, serves an ideal platform for the large-scale optical phased array. This section will first discuss the CMOS-compatible silicon photonic fabrication platform on which the large-scale optical phased array is implemented. The experimental results of three different optical phased array systems are then presented, including the large-scale passive optical phased arrays, the active optical phased array, and the apodized optical antenna array.

A. Fabrication Platform

The fabrication platform of the large-scale silicon photonic circuit is the backbone of this optical phased array work as well as many other silicon photonic researches in our group. We used 300-mm silicon-on-insulator (SOI) wafers with 220 nm silicon device layer and 2 μm buried oxide (BOX) layer in a CMOS foundry with a customized CMOS-compatible silicon photonic process. Optical immersion lithography was utilized at 65-nm technology node. Two silicon etches, a shallow etch with 110 nm depth and a full silicon etch, were applied to define the geometry of the photonic structures. Two types of dopings, n and p, were used to form p-n junctions and resistors to enable devices such as electrooptic modulators [41] and thermo-optic heaters [42], *etc.* Each doping type had two doping levels, the light doping to create low-loss electrooptic structures such as the integrated thermo-optic heater and the heavy doping to bring in low-resistance contacts such as the silicon leads for the thermo-optic heater, as shown in Fig. 1(b). Two metal interconnection levels (Metal 1 and Metal 2) and two metal contact levels (Contact and Via), all made from copper, were used to provide on-chip electrical interconnections and external electrical testing interfaces (e.g. probing pads). Fig. 12(a) shows a fabricated active unit cell of the optical phased array using this CMOS-compatible silicon photonic process, where the nanoantenna and the integrated silicon heater are seen. The SEM was taken after dry-etching away the SiO₂ cladding, using the metal layers as a hard mask, to expose the silicon device. Note that the position of the silicon lead of the heater is shifted from the center of the adiabatic bend to increase the heater length, which is slightly different from the schematic in Fig. 1(d). Fig. 12(b) shows the cross section of a fabricated device on this platform, where a full silicon layer with 220 nm thickness and four metal layers are shown. A germanium layer is also available to make optical detectors. In addition to these conventional silicon photonic layers, this platform also offers three layers of silicon nitride for the hybrid integration of on-chip erbium doped lasers [43] and other silicon nitride photonic structures [44]. All of these layers can be seamlessly integrated on the same chip to form a complete silicon photonic system. Furthermore, CMOS electronic circuits can also be integrated with the photonic chip through methods such as wafer bonding [45], [46] to provide sophisticated electrical control over the silicon photonic circuits.

B. Large-scale Passive Optical Phased Arrays

Two passive optical phased arrays, a 64×64 array to generate the MIT-logo as simulated in Fig. 8(a) and a 32×32
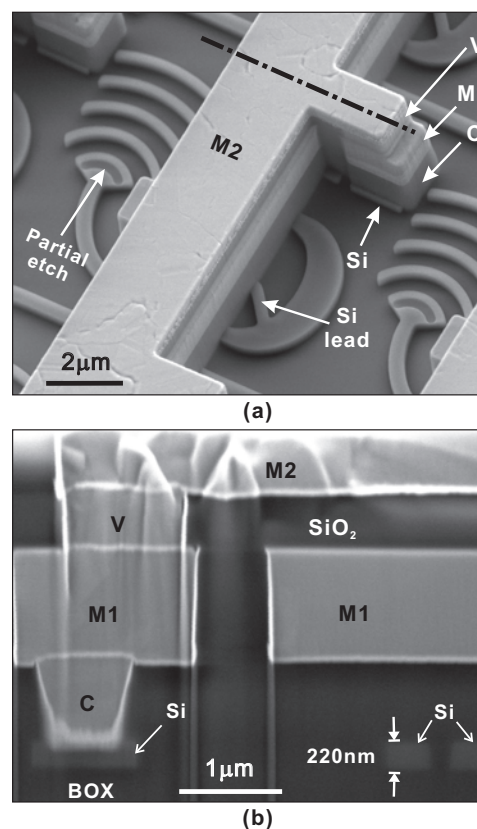

Fig. 12. (a) An SEM of the fabricated active unit cell of the optical phased array on the CMOS-compatible silicon photonic platform. (b) An SEM of the cross section of the fabricated antenna unit cell, where different layers are shown (C: Contact, V: Via, M1: Metal 1, M2: Metal 2). The cross section was taken at the silicon lead region of the thermo-optic heater, as indicated by the dash-dot line in (a).

array to create the multibeam pattern as simulated in Fig. 8(b), were fabricated with the CMOS-compatible silicon photonic process. Fig. 13(b) shows an SEM of part of the fabricated passive phased array. A transverse-electric (TE) polarized 1.55 μm laser was coupled into the silicon bus waveguide of the optical phased array, as illustrated in Fig. 1(a). The near-field emission and far-field radiation pattern were measured using the setup shown in Fig. 13(a), which is similar to that in [47]. The near-field emission was measured with the objective lens 1, as shown by the green rays in Fig. 13(a). The blue rays represent the light path of far-field imaging, where lens 1 projects the far-field image onto its back-focal plane (Fourier plane) which is then imaged by the infrared (IR) camera through lens 2. Fig. 13(c) shows the measured near-field emission of the 64×64 optical phased array, where uniform optical emission is observed across all of the 4,096 nanoantennas. Fig. 13(d) statistically analyzes the near-field intensity distribution, where the standard deviation is about 10% of the average intensity. The good uniformity of the near-field optical emission in such a large-scale system comes from the reliable directional coupler design as well as the precise CMOS processing techniques, providing an ideal interference condition where each nanoantenna contributes equally to the far-field interference. Fig. 13(f) shows the measured far-field radiation pattern of the 64×64 phased array, where the de-
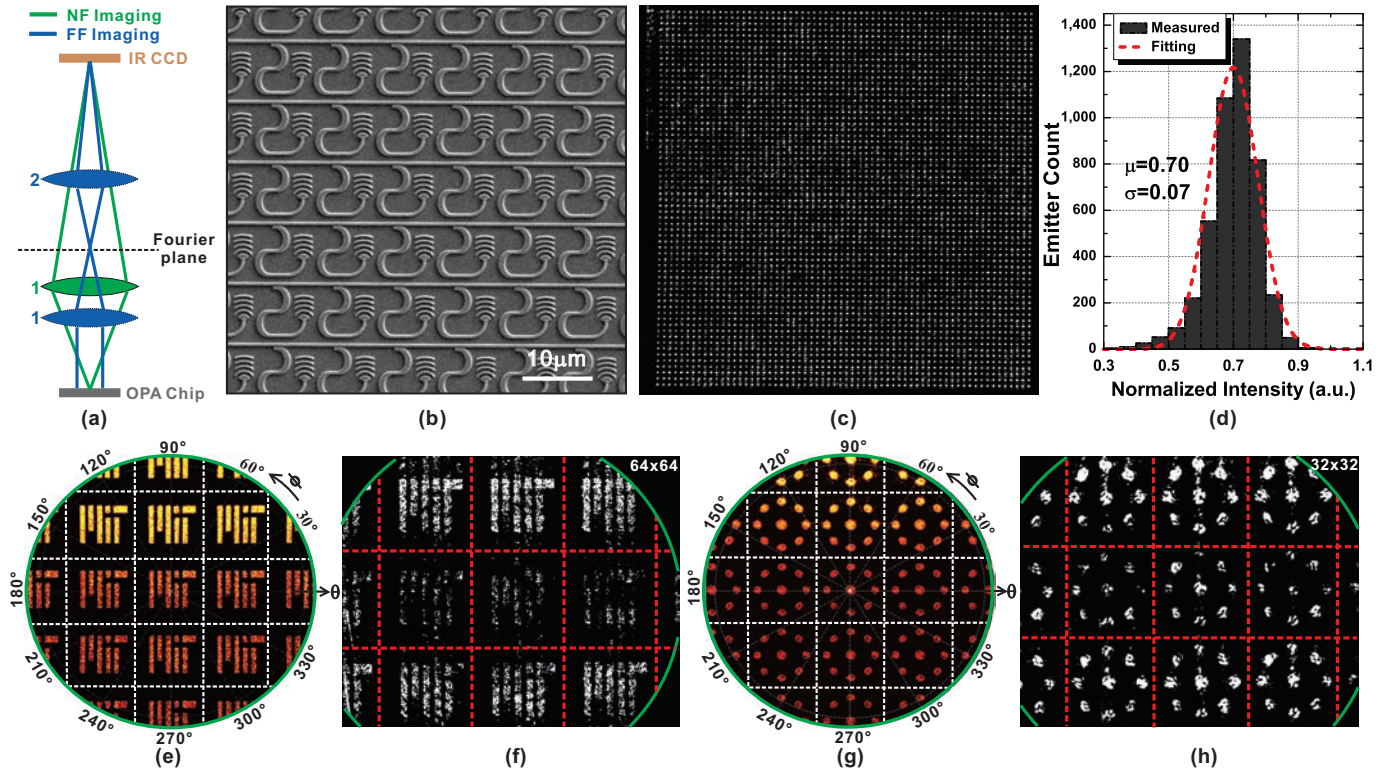
Fig. 13. Measurement results of the large-scale passive optical phased arrays. (a) The setup for the near-field (Green) and far-field (Blue) imaging. (b) An SEM of part of the fabricated 64×64 passive phased array. (c) Measured near-field optical emission of the 64×64 optical phased array. (d) Measured near-field intensity distribution of the 64×64 optical phased array. (e) The simulated far-field radiation pattern of the 64×64 phased array to form the MIT-logo, which is a close-up view of Fig. 11(b). The green circle corresponds to the numerical aperture of the objective lens, i.e. lens 1 in (a). (f) The measured far-field radiation pattern of the 64×64 optical phased array. (g) The simulated far-field radiation pattern of the 32×32 optical phased array to generate the multibeam pattern. (h) The measured far-field radiation pattern of the 32×32 optical phased array. The white and red lines in the images separate the interference orders. Figs. 13(a) and 13(e) reproduced with permission from [21], ©2013 NPG.

signed MIT-logo is generated. As predicted in Fig. 11, multiple interference orders are seen because the antenna spacing is greater than half of the optical wavelength. The far-field radiation pattern is clamped by the finite numerical aperture (0.4) of lens 1, as indicated by the green circle; therefore, only the optical emission with a small divergence angle from the vertical can be captured. Fig. 13(e) shows the corresponding simulated far field, which agrees well with the measurement. Fig. 13(g) and (h) show the simulated and measured far-field radiation of the 32×32 phased array for the multibeam pattern. A good agreement between simulation and experiment is again observed, which confirms the robustness of the optical phased array as we discussed in Section III-B.

Comparing the near-field emission in Fig. 13(c) with its far-field radiation pattern in Fig. 13(f), although the near-field emission contains no information but plain uniform emission, the far-field radiation pattern clearly delivers the information by reconstructing the designed image through the interference by thousands of optical antennas. In contrast with the conventional way of storing and transmitting images through the intensity of the pixels, the large-scale optical phased array opens up another way of imaging through the optical phase, like a hologram but generated from a single light input point. This demonstration, as a static optical phased array that is capable of generating truly arbitrary holographic patterns, will find immediate applications in, for example,

complex beamform generation [48] and spatial mode matching for optical space-division multiplexing [49], [50].

C. 8×8 Active Optical Phased Array

The large-scale phased array, in the passive form, has already shown remarkable capability to generate complex holographic patterns; however, it is preferable to have an active phased array in which the optical phase of the unit cells can be actively reconfigured to project dynamic patterns in the far field. This is accomplished by replacing the passive unit cells in the phased array with the active ones. Each active unit cell has a thermo-optically tunable phase shifter with a silicon heater directly integrated with the optical waveguide, as shown by the SEM in Fig. 12(a). Fig. 14(a) shows an SEM of the fabricated 8×8 active phased array. The tunable phase shifters in the same column are electrically connected to simplify the interconnection. Therefore, the optical phase of each column can be tuned together through the column heaters, and the phase of each row is adjusted by the row heater at the beginning of each row waveguide. Fig. 14(b) shows the simulated and measured near-field emission and far-field radiation of the 8×8 active phased array when no thermo-optic tuning was applied. Each nanoantenna was configured to emit with the same optical phase to create a focused beam in the far field. Also notice that side lobes exist around the main beam spot in each order.
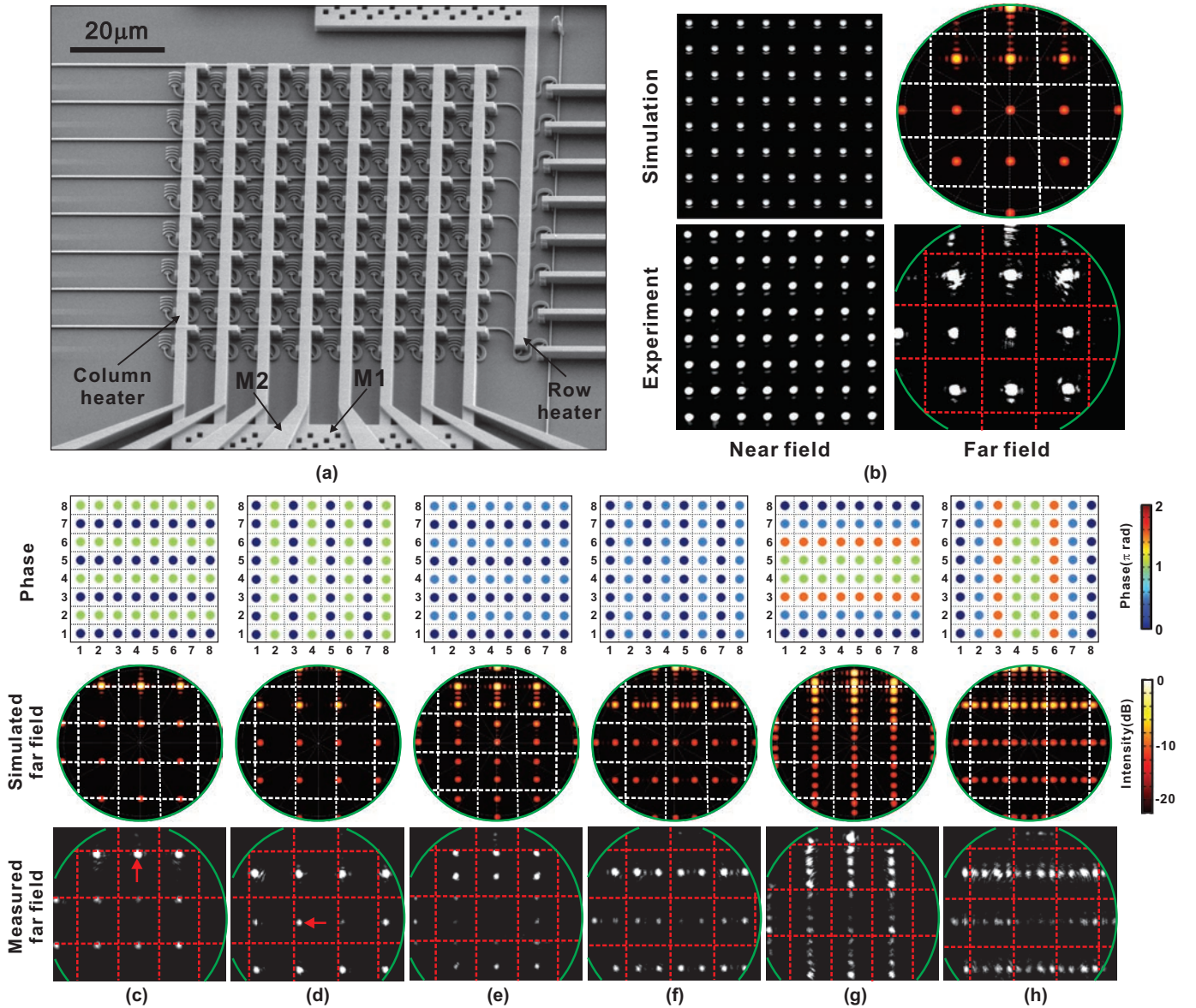
Fig. 14. Measurement results of the uniform 8×8 active optical phased array. (a) An SEM of the fabricated 8×8 active optical phased array with integrated silicon heaters in each unit cell and two-level metal interconnections. (b) The simulated and measured near-field emission and far-field radiation of the uniform 8×8 active optical phased array. Dynamic beamforming of the 8×8 active optical phased array by thermo-optically tuning the optical phase of the array so that the far-field optical beam can be (c) shifted in vertical and (d) in horizontal, (e) split into 2 beams in vertical and (f) in horizontal, and (g) split into 4 beams in vertical and (h) in horizontal. The corresponding phase distributions and simulated results are also shown.

By applying different heating power on the column heaters and row heaters, a variety of optical phase configurations can be achieved in the 8×8 phased array, and various radiation patterns can be dynamically generated in the far field, as shown in Fig. 14(c)-(h). It is seen the focused beam spot can be shifted, split into two beams, and split into four beams in two dimensions. The corresponding phase distributions and simulated far field are also shown. Good agreement between the simulation and the measurement is again observed. The measured thermo-optic efficiency is about 8.5 mW to achieve π phase shift in each unit cell, with an averaged temperature increase of about $\Delta T = 215°C$ across the ~20-µm waveguide in the unit cell. This high thermo-optic efficiency comes from the direct integration of the silicon heater with the

waveguide and is essential to the large-scale active phased array considering the large number of unit cells it contains.

Although only a small-scale 8×8 array is shown here, limited by the electrical control circuitry, it still represents the largest active optical phased array of its kind; moreover, this active phased array structure can be immediately extended to a larger scale with independent electrical control of each unit cell with the aid of a fully CMOS-controlled circuitry through, for example, wafer-boding with the photonic chip [46]. In this way, the large-scale active phased array can project dynamic, complex patterns in the far field with applications ranging from communication, 3D holographic displays to biomedical imaging.
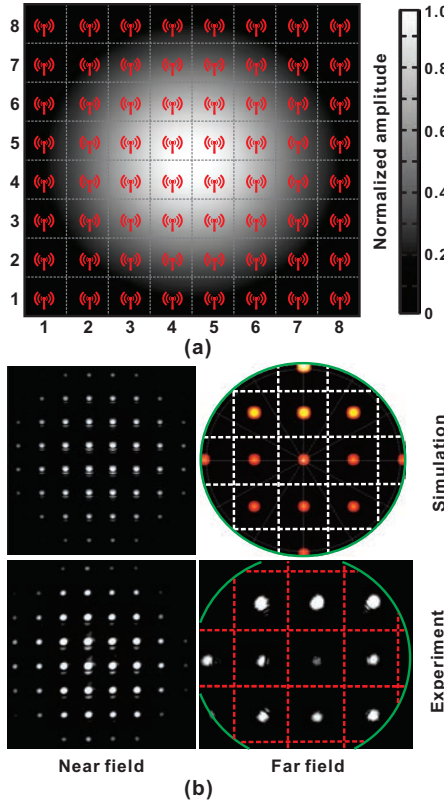
Fig. 15.   (a) The Gaussian-shaped apodization window of the 8×8 optical antenna array. (b) The simulated and measured near-field emission and far-field radiation of the apodized 8×8 optical antenna array. Note that some of the nanoantennas close to the edge are not visible in the near field.

D. Apodized Optical Antenna Array

In previous discussions, we focused mainly on the conventional phased array in the sense that its near-field optical emission is uniform across the whole array. Under certain circumstances, however, nonuniform near-field emission is preferred [51], [52]. For example, as we mentioned earlier, in the uniform optical phased array shown in Fig.14(b), undesired sidelobes are generated around the main beam spot in each order in the far field. According to the Fourier relation between the near and the far field, the sidelobes are caused by the uniform near-field emission window in which the optical emission is tuned off abruptly outside the phased array area. These unwanted sidelobes can be suppressed by tailoring the near-field emission with some slowly varying envelope function such as Gaussian, a common technique called apodization frequently used in other Fourier systems such as Bragg gratings. Fig. 15(a) shows such an apodized 8×8 optical antenna array in which the amplitude of the near-field emission is apodized with a Gaussian shape. The top-left panel of Fig. 15(b) simulates the corresponding near-field emission of the Gaussian-apodized array, where the intensity of the nanoantennas gradually fades away toward the edge of the array. This slowly varying Gaussian-shaped near-field emission window creates Gaussian-shaped optical beam in the far field according to the Fourier relation, which has no sidelobes, as shown by the simulation in the top-right
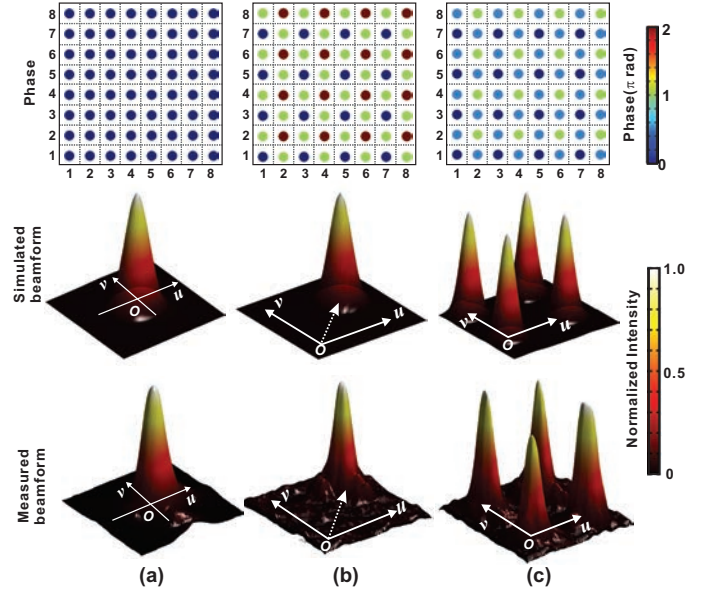

Fig. 16.   Dynamic far-field beamform generation with the apodized optical antenna array by actively tuning the phase of the nanoantennas. (a) The original Gaussian-shaped optical beam in the far field. (b) The beam shifts two-dimensionally. (c) The single beam splits into 2×2 beams. Note that only one interference order is shown, and point O in the images represents the center of the order.

panel of Fig. 15(b). The phased array architecture used in this work, where the directional couplers can be engineered to achieve arbitrary near-field optical emission profiles, is particularly suitable to make such non-uniform optical antenna arrays. The coupling coefficients corresponding to the optical emission profile can be calculated with (1) and (2), and then the coupler lengths and gaps can be obtained using Fig. 3(a). The bottom row of Fig. 15(b) shows the measured near-field emission and far-field radiation of the fabricated 8×8 optical antenna array with Gaussian apodization. It is seen the designed Gaussian-shaped near-field emission profile is achieved, and the sidelobes are successfully suppressed in the far field compared to the uniform array shown in Fig. 14(b). Good agreement between simulation and experiment is again observed, which confirms the robustness of the directional coupler design and the reliability of the advanced CMOS processing techniques.

Similar to the uniform phased array discussed in the last subsection, active phase tunability can be as well incorporated into the apodized antenna array so that the optical phase of the nanoantennas can be thermo-optically adjusted to project dynamic patterns in the far field. Fig. 16(a) shows the generated far-field beamform in one interference order of the apodized antenna array, where a Gaussian-shaped intensity profile is seen, as predicted. By applying different heating power on the integrated silicon heaters of the antenna array, the phase distribution can be reconfigured, and accordingly the single Gaussian beam in the far field can be shifted two-dimensionally (Fig. 16(b)) and can be split into 2×2 beams (Fig. 16(c)).

The demonstrated ability of the antenna array to engineer both the amplitude and phase of the near-field emission is of

particular importance in optical beamform generation where both the beam shape (amplitude) and the wavefront (phase) of the far-field beam need to be specified [52]. Furthermore, by introducing some active amplitude tuning component such as the germanium-based electro-absorption variable optical attenuator [53], [54], the near-field emission amplitude can also be dynamically reconfigured in the antenna array, which, combined with the demonstrated optical phase tunability, will enable the dynamic generation of truly arbitrary optical beamforms for a variety of applications such as optical spatial division multiplexing, optical trapping, *etc.*

V. CONCLUSION

The material and process compatibility gives silicon photonics access to the well-established, advanced CMOS processing technique that is not available to other photonic platforms such as indium-phosphide, and hence makes possible the large-scale photonic circuits to be made in a reliable and cost-effective way. As an example of such a large-scale silicon photonic circuit, we present in this paper the integrated optical phased arrays consisting of as many as 4,096 building blocks or 12,288 optical elements, representing the largest and densest silicon photonic integration demonstrated to date. Within the large number of integrated nanoantennas connected by optical waveguides, optical power can be arbitrarily distributed, and optical phase can be precisely aligned and actively adjusted to dynamically produce sophisticated interference patterns in the far field. This newly added capability to the optical phased array technology is expected to affect new fields such as communication, LADAR, three-dimensional holography, and biomedical sciences. Moreover, through this work, we can see the large-scale, system-level integrated silicon photonic circuitry has well and truly arrived.

REFERENCES

[1] K. F. Braun. (1909, Dec.) Nobel lecture: Electrical oscillations and wireless telegraphy. Stockholm, Sweden. [Online]. Available: http://www.nobelprize.org/nobel_prizes/physics/laureates/1909/braun-lecture.pdf

[2] T. F. Krauss, "Photonics: Phased array on a fingertip," *Nature*, vol. 493, no. 7431, pp. 170–171, Jan. 2013.

[3] A. J. Fenn, D. H. Temme, W. P. Delaney, and W. E. Courtney, "The development of phased-array radar technology," *Lincoln Lab. J.*, vol. 12, no. 2, pp. 321–340, 2000.

[4] M. Cherry, "Astronomy in south africa: The long shot," *Nature*, vol. 480, no. 7377, pp. 308–309, 2011.

[5] P. F. McManamon, T. A. Dorschner, D. L. Corkum, L. J. Friedman, D. S. Hobbs, M. Holz, S. Liberman, H. Q. Nguyen, D. P. Resler, and R. C. Sharp, "Optical phased array technology," *Proc. IEEE*, vol. 84, no. 2, pp. 268–298, 1996.

[6] R. A. Meyer, "Optical beam steering using a multichannel lithium tantalate crystal," *Appl. Opt.*, vol. 11, no. 3, pp. 613–616, Mar. 1972.

[7] D. P. Resler, D. S. Hobbs, R. C. Sharp, L. J. Friedman, and T. A. Dorschner, "High-efficiency liquid-crystal optical phased-array beam-steering," *Opt. Lett.*, vol. 21, no. 9, pp. 689–691, May 1996.

[8] W. R. Huang, J. Montoya, J. E. Kansky, S. M. Redmond, G. W. Turner, and A. Sanchez-Rubio, "High speed, high power one-dimensional beam steering from a 6-element optical phased array," *Opt. Exp.*, vol. 20, no. 16, pp. 17 311–17 318, Jul. 2012.

[9] N. W. Carlson, G. A. Evans, R. Amantea, S. L. Palfrey, J. M. Hammer, M. Lurie, L. A. Carr, F. Z. Hawrylo, E. A. James, C. J. Kaiser, J. B. Kirk, and W. F. Reichert, "Electronic beam steering in monolithic grating-surface-emitting diode laser arrays," *Appl. Phys. Lett.*, vol. 53, no. 23, pp. 2275–2277, 1988.

[10] M. Jarrahi, R. F. W. Pease, D. A. B. Miller, and T. H. Lee, "Optical switching based on high-speed phased array optical beam steering," *Appl. Phys. Lett.*, vol. 92, no. 1, p. 014106, 2008.

[11] T. K. Chan, M. Megens, B.-W. Yoo, J. Wyras, C. J. Chang-Hasnain, M. C. Wu, and D. A. Horsley, "Optical beamsteering using an 8×8 mems phased array with closed-loop interferometric phase control," *Opt. Exp.*, vol. 21, no. 3, pp. 2807–2815, Feb. 2013.

[12] D. Kwong, A. Hosseini, Y. Zhang, and R. T. Chen, "1×12 unequally spaced waveguide array for actively tuned optical phased array on a silicon nanomembrane," *Appl. Phys. Lett.*, vol. 99, no. 5, p. 051104, 2011.

[13] N. Yu, P. Genevet, M. A. Kats, F. Aieta, J.-P. Tetienne, F. Capasso, and Z. Gaburro, "Light propagation with phase discontinuities: Generalized laws of reflection and refraction," *Science*, vol. 334, no. 6054, pp. 333–337, 2011.

[14] F. Zhou, Y. Liu, and W. Cai, "Plasmonic holographic imaging with V-shaped nanoantenna array," *Opt. Exp.*, vol. 21, no. 4, pp. 4348–4354, Feb. 2013.

[15] W. Guo, P. Binetti, C. Althouse, M. Masanovic, H. Ambrosius, L. Johansson, and L. Coldren, "Two-dimensional optical beam steering with InP-based photonic integrated circuits," *IEEE J. Sel. Topics Quantum Electron.*, vol. 19, no. 4, pp. 6 100 212–6 100 212, 2013.

[16] R. A. Soref, "Silicon-based optoelectronics," *Proc. IEEE*, vol. 81, no. 12, pp. 1687–1706, 1993.

[17] R. A. Soref and B. Bennett, "Electrooptical effects in silicon," *IEEE J. Quantum Electron.*, vol. 23, no. 1, pp. 123–129, 1987.

[18] K. V. Acoleyen, H. Rogier, and R. Baets, "Two-dimensional optical phased array antenna on silicon-on-insulator," *Opt. Exp.*, vol. 18, no. 13, pp. 13 655–13 660, 2010.

[19] J. K. Doylend, M. J. R. Heck, J. T. Bovington, J. D. Peters, L. A. Coldren, and J. E. Bowers, "Two-dimensional free-space beam steering with an optical phased array on silicon-on-insulator," *Opt. Exp.*, vol. 19, no. 22, pp. 21 595–21 604, Oct. 2011.

[20] J. K. Doylend, M. J. R. Heck, J. T. Bovington, J. D. Peters, M. L. Davenport, L. A. Coldren, and J. E. Bowers, "Hybrid III/V silicon photonic source with integrated 1D free-space beam steering," *Opt. Lett.*, vol. 37, no. 20, pp. 4257–4259, Oct. 2012.

[21] J. Sun, E. Timurdogan, A. Yaacobi, E. S. Hosseini, and M. R. Watts, "Large-scale nanophotonic phased array," *Nature*, vol. 493, no. 7431, pp. 195–199, Jan. 2013.

[22] L. Chen, N. Sherwood-Droz, and M. Lipson, "Compact bandwidth-tunable microring resonators," *Opt. Lett.*, vol. 32, no. 22, pp. 3361–3363, Nov. 2007.

[23] F. Gan, T. Barwicz, M. Popović, M. Dahlem, C. Holzwarth, P. T. Rakich, H. Smith, E. Ippen, and F. Kärtner, "Maximizing the thermo-optic tuning range of silicon photonic structures," in *Proc. IEEE Photon. Switching Conf.*, 2007, pp. 67–68.

[24] P. Dong, R. Shafiiha, S. Liao, H. Liang, N.-N. Feng, D. Feng, G. Li, X. Zheng, A. V. Krishnamoorthy, and M. Asghari, "Wavelength-tunable silicon microring modulator," *Opt. Exp.*, vol. 18, no. 11, pp. 10 941–10 946, May 2010.

[25] C. T. DeRose, M. R. Watts, D. C. Trotter, D. L. Luck, G. N. Nielson, and R. W. Young, "Silicon microring modulator with integrated heater and temperature sensor for thermal control," in *Proc. Conf. Lasers Electro-Opt. (CLEO)*, 2010, p. CThJ3.

[26] M. Watts, W. Zortman, D. Trotter, G. Nielson, D. Luck, and R. Young, "Adiabatic resonant microrings (ARMs) with directly integrated thermal microphotonics," in *Proc. Conf. Lasers Electro-Opt. (CLEO)*, 2009, p. CPDB10.

[27] C. T. DeRose, M. Watts, R. W. Young, D. C. Trotter, G. N. Nielson, W. Zortman, and R. D. Kekatpure, "Low power and broadband 2×2 silicon thermo-optic switch," in *Proc. Opt. Fiber Commun. Conf. (OFC)*, 2011, p. OThM3.

[28] M. R. Watts, J. Sun, C. DeRose, D. C. Trotter, R. W. Young, and G. N. Nielson, "Adiabatic thermo-optic Mach-Zehnder switch," *Opt. Lett.*, vol. 38, no. 5, pp. 733–735, Mar. 2013.

[29] I. Shubin, X. Zheng, H. Thacker, J. Yao, J. Costa, Y. Luo, G. Li, A. V. Krishnamoorthy, J. E. Cunningham, T. Pinguet, and A. Mekis, "Thermally tunable soi cmos photonics circuits," pp. 76 070C–76 070C–6, 2010.

[30] M. R. Watts, "Adiabatic microring resonators," *Opt. Lett.*, vol. 35, no. 19, pp. 3231–3233, Oct. 2010.

[31] E. Timurdogan, M. Moresco, A. Biberman, J. Sun, W. Zortman, D. Trotter, and M. Watts, "Adiabatic resonant microring (ARM) modulator," in *Proc. IEEE Opt. Interconnects Conf. (OIC)*, 2012, pp. 48–49.

[32] A. Yaacobi, E. Timurdogan, and M. R. Watts, "Vertical emitting aperture nanoantennas," *Opt. Lett.*, vol. 37, no. 9, pp. 1454–1456, May 2012.

[33] P. Mühlschlegel, H.-J. Eisler, O. J. F. Martin, B. Hecht, and D. W. Pohl, "Resonant optical antennas," *Science*, vol. 308, no. 5728, pp. 1607–1609, 2005.

[34] L. Tang, S. E. Kocabas, S. Latif, A. K. Okyay, D.-S. Ly-Gagnon, K. C. Saraswat, and D. A. B. Miller, "Nanometre-scale germanium photodetector enhanced by a near-infrared dipole antenna," *Nat. Photon.*, vol. 2, no. 4, pp. 226–229, Mar. 2008.

[35] G. Roelkens, D. V. Thourhout, and R. Baets, "High efficiency silicon-on-insulator grating coupler based on a poly-silicon overlay," *Opt. Exp.*, vol. 14, no. 24, pp. 11 622–11 630, Nov. 2006.

[36] M. Fan, M. Popović, and F. X. Käertner, "High directivity, vertical fiber-to-chip coupler with anisotropically radiating grating teeth," in *Proc. Conf. Lasers Electro-Opt.(CLEO)*, 2007, p. CTuDD3.

[37] A. Taflove and S. Hagness, *Computational Electrodynamics: The Finite-Difference Time-Domain Method*, 3rd ed. Artech House, 2005.

[38] R. Haupt, *Antenna Arrays: A Computational Approach*. Wiley, 2010.

[39] R. W. Gerchberg and W. O. Saxton, "A practical algorithm for the determination of phase from image and diffraction plane pictures," *Optik*, vol. 35, pp. 237–246, 1972.

[40] J. R. Fienup, "Reconstruction of an object from the modulus of its Fourier transform," *Opt. Lett.*, vol. 3, no. 1, pp. 27–29, Jul. 1978.

[41] E. Timurdogan, C. Sorace-Agaskar, E. Hosseini, and M. Watts, "An interior-ridge silicon microring modulator," *J. Lightw. Technol.*, vol. PP, no. 99, pp. 1–1, 2013.

[42] M. Moresco, E. S. Hosseini, E. Timurdogan, D. D. Coolbaugh, G. Leake, and M. R. Watts, "Parallel-coupled adiabatic resonant microring (ARM) filter with integrated heaters," in *Proc. Conf. Lasers Electro-Opt.(CLEO)*, 2013, p. CTh1C.5.

[43] P. Purnawirman, J. Sun, T. N. Adam, G. Leake, D. Coolbaugh, J. D. B. Bradley, E. S. Hosseini, and M. R. Watts, "C- and L-band erbium-doped waveguide lasers with wafer-scale silicon nitride cavities," *Opt. Lett.*, vol. 38, no. 11, pp. 1760–1762, Jun. 2013.

[44] J. Sun, Purnawirman, E. S. Hosseini, J. D. B. Bradley, T. N. Adam, G. Leake, D. Coolbaugh, and M. R. Watts, "Uniformly spaced $\lambda/4$-shifted Bragg grating array with wafer-scale CMOS-compatible process," *Opt. Lett.*, vol. 38, no. 20, pp. 4002–4004, Oct. 2013.

[45] J. Burns, B. Aull, C.-L. Chen, C.-L. Chen, C. Keast, J. Knecht, V. Suntharalingam, K. Warner, P. Wyatt, and D.-R. Yost, "A wafer-scale 3-D circuit integration technology," *IEEE Trans. Electron Devices*, vol. 53, no. 10, pp. 2507–2516, 2006.

[46] L. Vivien, J. Osmond, D. Marris-Morini, P. Crozat, E. Cassan, J. M. Fédéli, S. Brision, J. F. Damlencourt, V. Mazzochi, and D. Van Thourhout, "European HELIOS project: Silicon photonic photodetector integration," in *Proc. IEEE Int. Conf. Group IV Photon.*, 2009, pp. 10–12.

[47] N. L. Thomas, R. Houdré, M. V. Kotlyar, D. O'Brien, and T. F. Krauss, "Exploring light propagating in photonic crystals with Fourier optics," *J. Opt. Soc. Am. B*, vol. 24, no. 12, pp. 2964–2971, Dec. 2007.

[48] I. Dolev, I. Epstein, and A. Arie, "Surface-plasmon holographic beam shaping," *Phys. Rev. Lett.*, vol. 109, p. 203903, Nov. 2012.

[49] N. Bozinovic, Y. Yue, Y. Ren, M. Tur, P. Kristensen, H. Huang, A. E. Willner, and S. Ramachandran, "Terabit-scale orbital angular momentum mode division multiplexing in fibers," *Science*, vol. 340, no. 6140, pp. 1545–1548, 2013.

[50] J. Wang, J.-Y. Yang, I. M. Fazal, N. Ahmed, Y. Yan, H. Huang, Y. Ren, Y. Yue, S. Dolinar, M. Tur, and A. E. Willner, "Terabit free-space data transmission employing orbital angular momentum multiplexing," *Nat. Photon.*, vol. 6, no. 7, pp. 488–496, Jul. 2012.

[51] J. Sun, D. B. Cole, A. Yaacobi, E. S. Hosseini, G. Leake, D. Coolbaugh, and M. R. Watts, "Two-dimensional apodized silicon photonic phased array," *Opt. Lett.*, submitted for publication.

[52] J. Sun, D. Cole, A. Yaacobi, E. Timurdogan, E. S. Hosseini, G. Leake, D. D. Coolbaugh, and M. R. Watts, "Optical beamform engineering using phase and amplitude coded nanophotonic antenna arrays," in *Proc. Conf. Lasers Electro-Opt.(CLEO)*, 2013, p. CTh5D.1.

[53] J. Liu, M. Beals, A. Pomerene, S. Bernardis, R. Sun, J. Cheng, L. C. Kimerling, and J. Michel, "Waveguide-integrated, ultralow-energy GeSi electro-absorption modulators," *Nat. Photon.*, vol. 2, no. 7, pp. 433–437, Jul. 2008.

[54] E. H. Edwards, L. Lever, E. T. Fei, T. I. Kamins, Z. Ikonic, J. S. Harris, R. W. Kelsall, and D. A. B. Miller, "Low-voltage broad-band electroabsorption from thin Ge/SiGe quantum wells epitaxially grown on silicon," *Opt. Exp.*, vol. 21, no. 1, pp. 867–876, Jan. 2013.

Jie Sun received the B.S. and M.S. degrees from Tsinghua Univeristy, Beijing, China, in 2007 and the Ph.D. degree from Massachusetts Institute of Technology (MIT), Cambridge, MA, in 2013, all in electrical engineering.

Since February 2013, he has been with the Research Laboratory of Electronics at MIT as a post-doctoral associate. He has previously worked at Bell Laboratories, Murray Hill, NJ, in 2010. His research interests are in the broad area of photonics, in particular, silicon photonic devices and on-chip systems for communication and other emerging applications, including their fabrication and integration techniques.

Dr. Sun is a recipient of the 2013 Dimitris N. Chorafas outstanding doctoral thesis award for his work on large-scale silicon photonic circuit. He is a member of the Optical Society of America (OSA).

Erman Timurdogan received the B.S. degree in electrical and electronics engineering from Koç University, Istanbul, Turkey, in 2010 and the M.S. degree in electrical engineering from MIT, Cambridge, MA, in 2013.

He has been with the Research Laboratory of Electronics at MIT since 2010. His current research focuses on modeling and testing integrated electro-optic and thermo-optic photonic devices and systems for low-power, high speed, wavelength division multiplexed (WDM) communications.

Mr. Timurdogan is a member of both the Institute of Electrical and Electronics Engineers (IEEE) and and OSA.

Ami Yaacobi received his B.S. degree in Electrical Engineering and BA in Physics with excellence in 2005 from the Technion, Haifa, Israel.

Since October 2010, he is studying for a Ph.D. in Material Science in MIT, conducting his research on optical phased arrays. Between 2005 and 2010 Ami worked as a system engineer in RAFAEL defense systems, Israel, designing electro-optical systems.

Zhan Su received the B.S. degree in physics from University of Science and Technology of China (USTC), Hefei, China, in 2011 and the S.M. degree in electrical engineering from MIT.

He has been with the Research Laboratory of Electronics at MIT since 2011. His research interests include optical filter design, polarization control in integrated photonics and high speed on-chip switches.

Mr. Su is a member of both OSA and IEEE.

Ehsan shah Hosseini received the B.S. degree in electrical engineering from Sharif University of Technology, Tehran, Iran in 2003 and the M.S. and Ph.D. degrees in electrical engineering from Georgia Institute of Technology, Atlanta, GA, in 2008 and 2011, respectively.

He has been with the Research Laboratory of Electronics at MIT since 2011 as a postdoctoral associate. His research interests include silicon photonics, biosensing, and solid state lasers.

Dr. shah Hosseini is a member of OSA and IEEE.

David B. Cole received the B.S. degree in physics from New York University, New York, NY, and the B.E. degree in electrical engineering from the Stevens Institute of Technology, Hoboken, NJ in 1996. He subsequently obtained the M.S. degree in electrical engineering from the University of Pennsylvania, Philadelphia, P.A. in 1998, followed by a M.B.A. in finance from the Wharton School in 2002.

He is currently a doctoral student at the Research Laboratory of MIT. He worked for Lockheed Martin as a radar and microwave engineer prior to business school. His current research interests are photonics with a particular interest in optical sensing and communications. He also maintains an interest in antenna and microwave engineering.

Mr. Cole is a member of IEEE, OSA, Tau Beta Pi, and Sigma Pi Sigma.

Michael R. Watts received the B.S. degree in electrical engineering from Tufts University, Medford, MA, in 1996. As a Draper Fellow, he received the S.M. and Ph.D. degrees in electrical engineering from MIT in 2001 and 2005, respectively.

He worked at the Charles Stark Draper Laboratory as a Member of Technical Staff in their Fiber Optics Group from 1996 to 1999. From 2005 to 2010, he was a Principal Member of Technical Staff at Sandia National Laboratories where he led their silicon photonics effort. In 2010, he returned to MIT as an Associate Professor in electrical engineering where he leads the Photonics Microsystem Group. His research focuses on photonic microsystems for low-power communications, sensing, and microwave-photonics applications. Professor Watts has over 100 authored or coauthored publications and over a dozen issued patents. His current interests include the modeling, fabrication, and testing of large-scale implementations of microphotonic circuits, systems, and networks that are being integrated, directly or through hybrid techniques, with CMOS electronics for high-speed transmitting, switching, and routing applications of digital signals. Additional interests include large-scale microphotonic sensing and imaging arrays, along with optical phased arrays, nanophotonic antennas, nonlinear optics, and manipulations of optical-electromagnetic fields on-chip.

Professor Watts is a member of both the Institute of Electrical and Electronics Engineers (IEEE) and the Optical Society of America (OSA).